



HAL
open science

A model of metal–silicate separation on growing planets

J. Monteux, Y. Ricard, N. Coltice, F. Dubuffet, M. Ulvrova

► **To cite this version:**

J. Monteux, Y. Ricard, N. Coltice, F. Dubuffet, M. Ulvrova. A model of metal–silicate separation on growing planets. *Earth and Planetary Science Letters*, 2009, 287 (3-4), pp.353-362. 10.1016/j.epsl.2009.08.020 . hal-01636042

HAL Id: hal-01636042

<https://uca.hal.science/hal-01636042>

Submitted on 18 Jan 2018

HAL is a multi-disciplinary open access archive for the deposit and dissemination of scientific research documents, whether they are published or not. The documents may come from teaching and research institutions in France or abroad, or from public or private research centers.

L'archive ouverte pluridisciplinaire **HAL**, est destinée au dépôt et à la diffusion de documents scientifiques de niveau recherche, publiés ou non, émanant des établissements d'enseignement et de recherche français ou étrangers, des laboratoires publics ou privés.

1 A Model of Metal-Silicate Separation on Growing Planets

2 J. Monteux^a, Y. Ricard^a, N. Coltice^a, F. Dubuffet^a, and M. Ulvrova^a

3 ^a *Université de Lyon, Lyon, F-69003, France ; Université Lyon 1, Lyon, F-69003, France ;*
4 *Ecole Normale Supérieure de Lyon, Lyon, F-69364, France ; CNRS, UMR5570, Laboratoire*
5 *de Sciences de la Terre, Villeurbanne, F-69622, France.*

6 Abstract

7 The thermal evolution of planets during their accretionary growth is strongly
8 influenced by impact heating. The temperature increase following a collision
9 takes place mostly below the impact location in a volume a few times larger
10 than that of the impactor. Impact heating depends essentially on the radius of
11 the impacted planet. When this radius exceeds ~ 1000 km, the metal phase
12 melts and forms a shallow and dense pool that penetrates the deep mantle
13 as a diapir. To study the evolution of a metal diapir we propose a model
14 of thermo-chemical readjustment that we compare to numerical simulations in
15 axisymmetric spherical geometry and with variable viscosity. We show that the
16 metallic phase sinks with a velocity of order of a Stokes velocity. The thermal
17 energy released by the segregation of metal is smaller but comparable to the
18 thermal energy buried during the impact. However as the latter is distributed
19 in a large undifferentiated volume and the former potentially liberated into a
20 much smaller volume (the diapir and its close surroundings) a significant heating
21 of the metal can occur raising its temperature excess by at most a factor 2 or 3.
22 When the viscosity of the hot differentiated material decreases, the proportion
23 of thermal energy transferred to the undifferentiated material increases and a
24 protocore is formed at a temperature close to that of the impact zone.
25 *Key words:* core formation; meteoritical impacts; early earth; numerical
26 modeling; differentiation.

27 1. Introduction

28 Core formation is the most important differentiation event that occurred dur-
29 ing Earth's history. Metal/silicates separation is a rapid event (< 60 My) (Yin
30 et al., 2002; Kleine et al., 2002; Touboul et al., 2007) contemporaneous with
31 Earth accretion and involving gravitational mechanisms such as percolation,
32 negative diapirism and Rayleigh-Taylor instabilities (Stevenson, 1990; Honda
33 et al., 1993). In the homogeneous accretion hypothesis, metal segregation and
34 thereby core formation need significant heating to exceed the melting temper-
35 ature of iron alloys or of silicates. During the early stages of planetesimals
36 formation, heating by decay of short lived radionuclides is a potential energy
37 source to enhance early differentiation (Yoshino et al., 2003). As a planetesimal
38 grows, its gravity increases and it will increasingly attract the other surrounding
39 planetesimals. The dissipation of the kinetic energy of the impacts provides a
40 later shallow source of heat.

41 Impacts of large planetesimals have strongly influenced the late accretionary
42 and thermal state of nearly fully-formed planetary bodies (Tonks and Melosh,
43 1992; Senshu et al., 2002). During an impact, when the relative velocity between
44 a planet and an impactor overcomes the seismic velocities of the medium, a shock
45 wave develops. The shock pressure is nearly uniform in a spherical region next
46 to the impact (the isobaric core), and strongly decays away from it (Croft, 1982;
47 Pierazzo et al., 1997). In this isobaric core, the kinetic energy of the impact
48 is dissipated and leaves a temperature anomaly of several hundred degrees on
49 Moon to Mars size bodies (Senshu et al., 2002; Monteux et al., 2007). The
50 temperatures reached are mostly related to the properties (density and radius)
51 of the impacted body, and only weakly to those of the impactor (Monteux et al.,
52 2007). The melting temperature of iron alloys is lower than the silicates solidus
53 (Fei et al., 1997; Agee, 1997; Ghosh and McSween, 1998). On large impacted

54 planets, a local differentiation may occur between heavy metal and light silicates
55 in the heated anomaly (Tonks and Melosh, 1992). Hence, a thermo-chemical
56 readjustment follows, associated with the sinking of the metallic component
57 toward the center of the impacted protoplanet (Fig. 1).

58 For large planets, gravitational energy release due to core formation can
59 induce melting of the whole planet (Stevenson, 1989; Ricard et al., 2009). This
60 subsequent melting depends on the mechanisms of the metal descent (Samuel
61 and Tackley, 2008; Golabek et al., 2008). The aim of this study is to determine
62 the thermal evolution of metal during descent and the thermal state of the core.

63 First, we propose analytical and numerical isoviscous models of segregation
64 of a purely spherical iron diapir. As the viscosity contrast between molten metal
65 and undifferentiated cold material can reach several orders of magnitude, we
66 then focus on more realistic models of segregation of metal after a large impact
67 with temperature dependent rheologies. We show that the size of impactors and
68 viscosities involved largely determine the inner thermal state of a young planet.

69 **2. Thermo-chemical state after large impact**

70 *2.1. Thermal state*

71 After a meteoritical impact, heating is localized in a spherical region called
72 the isobaric core just beneath the impact site. The radius of the isobaric core
73 R_{ic} is comparable to the radius of the impactor R_{imp} and depends on en-
74 ergy conversion during the shock. With a minimal set of assumptions, we get
75 $R_{ic} = 3^{1/3} R_{imp}$ following Senshu et al. (2002) and Pierazzo et al. (1997). Just
76 after the adiabatic pressure release, the isobaric core is isothermal and we call
77 ΔT_0 the shock induced temperature increase. The lower script 0 indicates that
78 we consider this instant as the origin of our time variable. Outside the isobaric
79 core, the temperature anomaly decays as $\Delta T_0(r) = \Delta T_0 (R_{ic}/r)^m$ with $m \sim 4.4$

80 as proposed by Senshu et al. (2002). Assuming that the kinetic energy of the
 81 impactor is controlled by the escape velocity of the impacted body and that
 82 impactor and impacted body have the same densities (i.e., $\rho_{ic} = \rho_{imp} \equiv \rho_0$), a
 83 simple energy balance (see e.g., Monteux et al., 2007), indicates that

$$\Delta T_0 = \frac{4\pi}{9} \frac{\gamma}{h(m)} \frac{\rho_0^2 G R^2}{\overline{\rho C_p}}, \quad (1)$$

84 where $\overline{\rho C_p}$ is the average heat capacity of the impacted body that is plausibly a
 85 mixture of silicate and metal, G is the gravitational constant, ρ_0 is the density of
 86 the undifferentiated material, R is the radius of the impacted planet and where
 87 the function $h(m)$ represents the volume effectively heated normalized by the
 88 volume of the isobaric core (typically $h(m) \sim 2 - 3$ (Monteux et al., 2007)).
 89 The empirical coefficient γ is the fraction of the kinetic energy of the impactor
 90 dissipated as heat. From shock experiments, γ ranges between 0.2 and 0.4 de-
 91 pending on material properties and shock velocities (O’Keefe and Ahrens, 1977)
 92 (i.e., 20 to 40% of the kinetic energy is buried at depth, the rest rapidly radiated
 93 away during or shortly after the impact). The shock-induced temperature ex-
 94 cess, ΔT_0 , strongly increases with the radius of the impacted body. According
 95 to the set of parameters of Table 1, $\Delta T_0(\text{K}) = 4.7 \times 10^{-5} R^2(\text{km})$; for a Moon
 96 size body ΔT_0 is 140 K while it is 1925 K for an Earth size body.

97 The thermal state of a protoplanet before an impact depends on its growth
 98 history and on its initial heating caused by short lived radionuclides like ^{26}Al
 99 and ^{60}Fe . This early radioactive heating can eventually cause melting and differ-
 100 entiation of planetesimals that have quickly grown (Yoshino et al., 2003). The
 101 impact heating superimposed to a sufficiently hot protoplanetary interior can
 102 trigger melting of the Fe-FeS system (the eutectic temperature is close to 1250
 103 K at 1 bar) (Fei et al., 1997) and potentially of silicates (solidus temperature is
 104 around 1500 K at 1 bar) (Agee, 1997). In these cases, a fraction of the thermal

105 energy is converted to latent heat during the phase transformations.

106 *2.2. Compositional state*

107 An impact on a large enough undifferentiated protoplanet composed of a
108 mixture of metals and silicates can trigger phase transformations and initiate
109 differentiation. The first component that melts is the metal phase. In the region
110 where metal melting occurs, the liquid metal can percolate through the solid
111 silicate matrix. Percolation is only possible for small dihedral angles ($< 60^\circ$)
112 or for large melt volume fraction above a percolation threshold. The dihedral
113 angle of liquid iron alloy within silicates is large ($\sim 100^\circ$) in the upper mantle
114 but decreases with increasing pressure (Shannon and Agee, 1996). However,
115 the volume fraction of liquid alloy is typically larger than 10% if melting is
116 complete, which overcomes the percolation threshold (Von Bagen and Waff,
117 1986). On Earth the core represents 17% of the volume of the planet, Mars has
118 likely a slightly smaller core but Mercury's core is 43% of the planet. The metal
119 is collected at the bottom boundary of the melted zone forming a diapir that
120 ultimately sinks within the interior of the impacted protoplanet (Ricard et al.,
121 2009).

122 If the temperature exceeds the silicate solidus and eventually the liquidus,
123 the separation of metal and silicates can occur as a metal rainfall through a
124 turbulent magma (Stevenson, 1990; Höink et al., 2005). Small droplets of heavy
125 metal sediment at the bottom of the melted region. This scenario may not be
126 the generic one, as it would imply that a planet embryo maintains a melted
127 metal component without differentiating until the silicates start melting. It has
128 been suggested that the metal may segregate per percolation, as soon as it melts,
129 while the silicates are still mostly solid (Ricard et al., 2009). Locally, however,
130 the impact of an undifferentiated planetesimal on an already differentiated large
131 planetary embryo, may of course, be energetic enough to melt (or even vaporize)

132 the silicate and metal contents of the impactor and the silicates of the impacted
133 body inside the isobaric core.

134 The two processes (percolation or metal “rain”) lead to a local differentiation
135 within the melted region between light silicates and heavy metals on a short
136 timescale compared to that of the slow viscous deformation (Tonks and Melosh,
137 1992). The melted region is as large as or a few times larger than the isobaric
138 core (Pierazzo et al., 1997). Here, we identify the initially differentiated zone to
139 the isobaric core, metal being overlaid by pure silicates shortly after the impact
140 (see Fig.1).

141 **3. Dynamic model of differentiation**

142 The setting described in the previous section is gravitationally unstable and
143 the metal phase sinks toward the center of the impacted planetesimal while the
144 silicates (lighter than undifferentiated material) spread underneath the surface.
145 To study the global dynamics of this differentiation event, we develop a thermo-
146 mechanical model in spherical axisymmetrical geometry, of viscous flow with
147 three chemical components. Using a viscous and linear rheology during the
148 segregation of the core is clearly a large approximation. The large deviatoric
149 stress generated by the metallic diapirs should lead to a non-linear rheology
150 (Samuel and Tackley, 2008), elasto-plastic deformations (Gerya and Yuen, 2007)
151 or even to hydrofracturation if they exceed the ultimate strength of rocks which
152 is $\sim 1 - 2$ GPa (Davies, 1982). Pressure dependence of the rheology can also
153 influence the metal sinking time but is not considered here since we focus on
154 small growing planets. During the early stages of accretion, the interior of the
155 growing planets may have been colder or hotter than the outer layers depending
156 on the ratio of radioactive and impact heating and on the history of accretion.
157 For simplicity, we assume in our models an homogenous temperature on the

158 growing planet before the impact.

159 3.1. Physical model

160 Sinking occurs under the action of gravity in a spherical homogeneous pro-
161 toplanetary body. We neglect for simplicity the changes of gravity during the
162 differentiation. Hence gravitational acceleration $g(r)$ increases linearly with ra-
163 dius r :

$$g(r) = \frac{4}{3}G\pi\rho_0r = g_0\frac{r}{R}, \quad (2)$$

164 where g_0 the surface gravity. The density of undifferentiated material is $\rho_0 =$
165 $f_0\rho_{Fe} + (1 - f_0)\rho_{Si}$ where f_0 is the volume fraction of metal and ρ_{Fe} , ρ_{Si} , the
166 densities of the metallic phase and the pure silicates, respectively (see typical
167 numerical values in Table 1.)

168 The dynamics of segregation potentially involves a series of multiscale physi-
169 cal processes, especially to take the effects of melting into account and a realistic
170 multiphase dynamics (Golabek et al., 2008; Ricard et al., 2009). No numerical
171 models can handle simultaneously all these complexities and as a consequence,
172 we follow the approach of Samuel and Tackley (2008) and consider a thermo-
173 chemical system with infinite Prandtl limit, with no possible subsequent phase
174 separation within the undifferentiated material except that caused by the im-
175 pact (e.g., the volumes of pure metal and pure silicates remain constant during
176 the simulations and equal to 17% and 83% of the initial isobaric core).

177 The necessary approximations are somewhat different from the classic treat-
178 ment of thermal convection (see e.g., Ricard, 2007). We non-dimensionalize the
179 lengths by the planetary radius R , the velocities by a Stokes velocity $\Delta\rho_0g_0R^2/\eta_0$
180 (where $\Delta\rho_0 = \rho_{Fe} - \rho_{Si}$ and η_0 is the reference viscosity of cold material far from
181 the impact site), the temperature by ΔT_0 (see Eq.1). The governing mechanical
182 non-dimensionnal equations are the conservation of mass

$$\nabla \cdot \mathbf{v} = 0, \quad (3)$$

183 and the conservation of momentum

$$-\nabla P + \nabla \cdot \left(\frac{\eta}{\eta_0} \left[\nabla \mathbf{v} + [\nabla \mathbf{v}]^T \right] \right) + \left(\frac{T}{B} - f \right) r \mathbf{e}_r = 0, \quad (4)$$

184 where \mathbf{v} , P , T and r are the non-dimensional velocity, pressure, temperature
 185 and radius, η the viscosity, T_0 the temperature (assumed uniform) before the
 186 impact and \mathbf{e}_r the radial unit vector. The buoyancy ratio B (Christensen and
 187 Yuen, 1985) is:

$$B = \frac{\Delta \rho_0}{\rho_0 \alpha \Delta T_0}. \quad (5)$$

188 The downward buoyancy force that drives the flow increases with the volume
 189 fraction of metal f that varies between 0 (pure silicates) and 1 (pure metal),
 190 0.17 being that of undifferentiated material. A depth dependent and constant
 191 in time gravity has been used in the momentum equation Eq.4 although, in
 192 principle, gravity should have been computed self-consistently from the time-
 193 dependent density distribution. We assume a temperature dependent viscosity
 194 such as $\eta = \eta_0 \lambda^T$ with λ being the viscosity factor (lower than 1) which is
 195 equivalent to the viscosity ratio between the hottest and coldest material at the
 196 start of the experiment. Such a viscosity decreases sharply with temperature
 197 and is simpler to implement than the usual Arrhenius law (Ratcliff et al., 1997;
 198 Ziethe and Spohn, 2007).

199 The conservation of energy writes

$$\frac{DT}{Dt} = \frac{\nabla^2 T}{Ra_x} + D_x \frac{\eta}{\eta_0} \Phi + \frac{1}{B} \frac{\Delta \rho}{\rho} \frac{T}{\Delta T_0} D_x \frac{DP}{Dt}. \quad (6)$$

200 The importance of diffusion is controlled by the compositional Rayleigh num-

201 ber Ra_χ ,

$$Ra_\chi = \frac{\Delta\rho_0 g_0 R^3}{\kappa\eta_0}, \quad (7)$$

202 the chemical dissipation number is

$$D_\chi = \frac{\Delta\rho_0 g_0 R}{\rho C_p \Delta T_0}, \quad (8)$$

203 considering for simplicity that $\overline{\rho C_p} = \rho_{Fe} C_p^{Fe} = \rho_{Si} C_p^{Si}$ (truly, see Table 1,
 204 $\rho_{Fe} C_p^{Fe} = 4 \times 10^3 \text{ kJ K}^{-1} \text{ m}^{-3}$, $\rho_{Si} C_p^{Si} = 3.85 \times 10^3 \text{ kJ K}^{-1} \text{ m}^{-3}$, and we use
 205 $\overline{\rho C_p} = 4 \times 10^3 \text{ kJ K}^{-1} \text{ m}^{-3}$). As g_0 is proportional to R and ΔT_0 to R^2 , see
 206 Eq.1, the chemical dissipation is independent of the planet radius and amounts
 207 to 36.6 (see Table 1).

208 An important energy source is provided by the dimensionless dissipation
 209 function Φ that expresses the conversion of potential energy into heat

$$\Phi = 2 \underline{\epsilon} : \underline{\epsilon}. \quad (9)$$

210 where $\underline{\epsilon}$ is the dimensionless strain rate tensor. For simplicity, we make the
 211 approximation that the thermal conductivities of the metal, silicates and undif-
 212 ferentiated materials are the same (truly $k_{Fe}=10 \text{ W m}^{-1} \text{ K}^{-1} > k_{Si}=3 \text{ W m}^{-1}$
 213 K^{-1}).

214 The metal volume fraction is then simply advected by the flow,

$$\frac{Df}{Dt} = 0. \quad (10)$$

215 3.2. Model approximations

216 The equations of momentum and energy conservations, Eq.4 and Eq.6, are
 217 similar to those classically used for mantle convection simulation but a number
 218 of differences should be discussed. As the buoyancy number B is very large (the

219 density difference between metal and silicates is 40 to 620 times larger than the
220 thermal density variations), the thermal buoyancy T/B can be safely neglected
221 in the momentum equation.

222 Neglecting the terms in $1/B$ implies to omit the adiabatic heat transfer
223 (the term in (DP/Dt)) in Eq.6 but to keep the dissipation term $D_\chi(\eta/\eta_0)\Phi$.
224 The differentiation of the planet liberates a large amount of potential energy
225 converted into heat by the dissipation term but the adiabatic heating remains
226 small. This is very different from the typical convection situation in which
227 there is no time variation of the potential energy, and where the dissipation is
228 on average, balanced by the work due to compression and expansion over the
229 convective cycle (Hewitt et al., 1975).

230 *3.3. Numerical model*

231 We implement a finite volume numerical model to solve Eq.3, Eq.4, Eq.6
232 and Eq.10 in axi-symmetric spherical geometry. We use a stream function for-
233 mulation for the equations of motion with a direct implicit inversion method
234 (Schubert et al., 2001). Eq.6 and Eq.10 are solved by an Alternating Direc-
235 tion Implicit (ADI) scheme (Peaceman and Rachford, 1955; Douglas, 1955).
236 The stream function, temperature and compositional fields are described by a
237 second-order approximation in space. To limit numerical diffusion when solving
238 the transport equations, especially for the compositional field, we use a Total
239 Variation Diminishing Superbee scheme (Roe, 1986; Laney, 1998) implemented
240 in an implicit way (Sramek, 2007) which enables a high resolution of pure advec-
241 tive fields. We use at least 200×200 grid points. Velocity boundary conditions
242 are free-slip at the surface and along the symmetry axis. Thermal boundary con-
243 ditions are isothermal at the surface and insulating along the symmetry axis.
244 We benchmark the viscous flow solver with variable viscosity and the transport
245 scheme against several analytical solutions (Monteux, 2009).

246 **4. Thermal evolution of sinking metallic diapir: Analytical consider-**
 247 **ations**

248 Before showing the results of complex numerical simulations with temper-
 249 ature dependent rheologies, we develop a simple model describing the thermal
 250 evolution of the sinking metal diapir, by approximating the metal diapir by a
 251 spherical drop falling into undifferentiated medium of uniform viscosity with
 252 a Stokes-like velocity. The radius of the metal drop R_{Fe} , can be related to
 253 the radius R_{ic} of the volume initially differentiated after impact heating, by
 254 $R_{Fe}^3 = f_0 R_{ic}^3$ and to the radius of the impactor by $R_{Fe}^3 = 3f_0 R_{imp}^3$.

255 *4.1. Sinking velocity*

256 The velocity V of the metallic diapir in an undifferentiated medium is compa-
 257 rable to the Stokes velocity of a sphere of similar volume. The density difference
 258 between the metal and the undifferentiated material is a function of tempera-
 259 ture and composition but the temperature contribution is minor. Hence, we
 260 consider $\Delta\rho = (1 - f_0)\Delta\rho_0$. Because gravity is a linear function of depth, the
 261 velocity of the sphere decreases during sinking as

$$V = \frac{dr}{dt} = -c_1(1 - f_0) \frac{\Delta\rho_0 g_0 R_{Fe}^2}{\eta_S} \frac{r}{R}. \quad (11)$$

262 In equation Eq.11, the dimensionless constant c_1 depends on the geometry of
 263 the system and on the viscosity contrast between the falling sphere and the
 264 surrounding medium.

265 The viscosity of the surrounding undifferentiated material η_S controls the
 266 sinking velocity. In the case of a sphere sinking in an infinite medium, the
 267 coefficient c_1 is given by the Hadamard-Rybczynski equation and varies from
 268 $4/15 = 0.27$ (isoviscous) to $1/3 = 0.33$ for an inviscid sphere (Hadamard, 1911;
 269 Rybczynski, 1911). In the situation described in this paper, the boundary condi-

270 tions are applied at a finite distance (the planetary surface) and the Hadamard
 271 and Rybczynski equation is thus only an approximation (Honda et al., 1993;
 272 Samuel and Tackley, 2008). The exact value of the constant c_1 will be obtained
 273 later through numerical experiments.

274 The position of the metallic drop obtained by solving Eq.11 varies from an
 275 initial position r_0 ($r_0 = R - R_{Fe} \sim R$) as

$$r(t) = r_0 \exp\left(-\frac{t}{\tau_S}\right), \quad (12)$$

276 with a characteristic time equal to

$$\tau_S = \frac{\eta_S R}{c_1 \Delta \rho_0 g_0} \frac{1}{(1 - f_0)} \frac{1}{R_{Fe}^2}. \quad (13)$$

277 As g_0 is proportional to the planetary radius R (Eq.2), the time τ_S is inde-
 278 pendent of the planetary radius but depends only on the diapir size R_{Fe} . Of
 279 course, no segregation occurs, i.e., $\tau_S \rightarrow +\infty$, for a planet of pure silicates
 280 ($f_0 = 0$ which means $R_{Fe} = 0$) or of pure metal ($f_0 = 1$). This characteristic
 281 sinking time is strongly dependent of the viscosity of the surrounding undiffer-
 282 entiated material which is poorly constrained. With the typical values of Table
 283 1, this time can be computed from the size R_{imp} of the impactor and we find
 284 $\tau_S(\text{kyr}) = 2.7 \times 10^9 (\eta_S / \eta_0) R_{imp}^{-2} (\text{km})$.

285 4.2. Global energy conversion

286 As we assume that gravity remains constant with time (albeit non-uniform),
 287 the energy equation Eq.6 integrated over the whole planet with the use of the
 288 momentum equation Eq.4 and neglecting the adiabatic decompression of the
 289 planet during the core segregation is simply

$$\frac{d}{dt}(\Delta E_p + \Delta E_T) = F, \quad (14)$$

290 where the total potential and thermal energies changes are

$$\Delta E_p = \int_{\Omega} \frac{1}{2} [\rho(\mathbf{r}, t) - \rho(\mathbf{r}, 0)] g_0 \frac{r^2}{R} dV, \quad (15)$$

291 (Ω is the planetary volume),

$$\Delta E_T = \int_{\Omega} \overline{\rho C_p} [T(\mathbf{r}, t) - T(\mathbf{r}, 0)] dV, \quad (16)$$

292 and the heat flux F is ,

$$F = \int_{\Sigma} k \frac{\partial T}{\partial r} dS, \quad (17)$$

293 (Σ is the planetary surface).

294 As we neglect the term in $1/B$ in the energy equation Eq.4, the budget Eq.14
 295 misses the energy variation ΔE_a due to the changes in pressure (the subscript
 296 a means that this term is related to changes in adiabatic compression)

$$\frac{d\Delta E_a}{dt} = \int_{\Omega} \alpha T \frac{\partial P}{\partial t} dV \sim \alpha T_0 \frac{d}{dt} \int_{\Omega} [P(\mathbf{r}, t) - P(\mathbf{r}, 0)] dV \quad (18)$$

297 (where the last approximation assumes that the temperature remains close
 298 to T_0). The difference of pressure between a homogeneous and a differentiated
 299 planet is easy to compute analytically and is of order $\alpha T_0 \Delta E_p$, i.e., a few percent
 300 of the changes in potential energy. This confirms that the energy change due to
 301 pressure changes is a minor effect.

302 4.3. Maximum temperature

303 The maximum temperature that the sinking metal can reach can be esti-
 304 mated by assuming that the whole variation of potential energy is only used to
 305 heat up the metal, without any heat transfer to the surrounding material.

306 Let us consider a melted zone of radius R_{ic} underneath and tangent to the
 307 planetary surface that differentiates ultimately forming a metallic core of volume
 308 V_{Fe} and radius R_{Fe} (with $R_{Fe}^3 = f_0 R_{ic}^3$) and a silicate layer of volume V_{Si} within
 309 a shell surrounding the whole planet with inner shell radius R_S and outer shell
 310 radius R i.e., $R_S^3 = R^3 - (1 - f_0) R_{ic}^3$. The change of potential energy is according
 311 to Eq.15 (see also Flasar and Birch, 1973):

$$\Delta E_p = \frac{2\pi}{5R} g_0 ((\rho_{Fe} - \rho_0) R_{Fe}^5 + (\rho_{Si} - \rho_0) (R^5 - R_S^5)). \quad (19)$$

312 Assuming $R_{ic} \ll R$, a Taylor expansion of Eq.19 leads to

$$\Delta E_p \sim -\frac{1}{2} \Delta \rho_0 g_0 R f_0 (1 - f_0) V_{ic} = -\frac{1}{2} (\rho_{Fe} - \rho_0) g_0 R V_{Fe} = -\frac{1}{2} (\rho_0 - \rho_{Si}) g_0 R V_{Si}, \quad (20)$$

313 where V_{ic} is the volume of the isobaric core. The change of potential energy
 314 is thus equivalent to that released by the sinking of the isobaric volume V_{ic}
 315 and excess density $f_0(1 - f_0)\Delta\rho_0$. Alternatively it corresponds to the energy
 316 released by a metal sphere of volume V_{Fe} sinking, or of a silicate sphere rising,
 317 through undifferentiated material. If only the metal heats up, the change of
 318 thermal energy according to Eq.16 is $\Delta E_T = \overline{\rho C_p} f_0 \Delta \Theta V_{ic}$ where $\Delta \Theta$ is the
 319 temperature increase (just after the impact, the metal temperature is $T_0 + \Delta T_0$,
 320 then it reaches at most $T_0 + \Delta T_0 + \Delta \Theta$). A scaling value for the temperature
 321 increase during segregation is thus

$$\Delta \Theta = \frac{1 - f_0}{2} \frac{1}{\overline{\rho C_p}} \Delta \rho_0 g_0 R. \quad (21)$$

322 As g_0 is proportional to R (Eq.2), the core segregation can increase the tem-
 323 perature by a quantity proportional to R^2 (in agreement with Flasar and Birch,
 324 1973; Ricard et al., 2009). The ratio of $\Delta \Theta$ to the post impact temperature

325 ΔT_0 is, according to Table 1 and Eq.1,

$$\frac{\Delta\Theta}{\Delta T_0} = \frac{3h(m)}{2\gamma}(1 - f_0)\frac{\Delta\rho_0}{\rho_0} \sim 11.8 \quad (22)$$

326 or, $\Delta\Theta(\text{K}) = 11.8 \Delta T_0(\text{K}) = 5.6 \times 10^{-4} R^2(\text{km})$ which rapidly becomes a large
 327 quantity as R increases. Of course, in a real situation not all energy will remain
 328 within the metal, and we will see that, when the metal diapir is too small, the
 329 metal can even cool off rather than warm up during its motion.

330 4.4. Thermal regime of the metallic sphere

331 While the hot metallic sphere is sinking, it warms up by shear heating but
 332 it also cools down by diffusion. In the reference frame of the sinking drop, the
 333 conservation of energy integrated over the volume V_{Fe} of the metallic drop (or
 334 through its surface S_{Fe}) indicates that

$$\overline{\rho C_p} V_{Fe} \frac{d\Delta T}{dt} = -k \frac{\Delta T}{\delta} S_{Fe} + \underline{\tau} : \nabla \mathbf{v} V_{Fe}, \quad (23)$$

335 where we assume that the temperature and the dissipation are at first order
 336 uniform in the metal. The difference ΔT is the difference between the diapir
 337 and the undifferentiated material. We assume that $\Delta T = T - T_0$, i.e., that
 338 the hot diapir sinks into a medium that keeps its initial temperature outside
 339 the boundary thickness δ . Even when the diapir viscosity is low and when the
 340 dissipation occurs significantly outside it, our numerical simulations shows that
 341 the maximum temperature is reached inside the diapir.

342 The thickness δ over which the temperature diffuses should be written as R_{Fe}
 343 times a dimensionless function c_2 of the various parameters of the problem. The
 344 thickness of the diffusive boundary layer, c_2 , should decrease with the sinking
 345 velocity of the diapir (i.e., with the Peclet number VR_{Fe}/κ) as a power law
 346 with exponent $-1/2$ or $-1/3$, depending on the viscosity ratio between the metal

347 and the undifferentiated material (see e.g., Ribe, 2007). We can also write the
 348 dissipation $\underline{\tau} : \nabla \mathbf{v} = \eta_e V^2 / R_{Fe}^2$ where η_e is the effective viscosity of the region
 349 where dissipation occurs. In this case, Eq.23 using the expressions of the time
 350 dependent position, Eq.12, and of the maximum temperature increase, Eq.21,
 351 can be recast as

$$\frac{d\Delta T}{dt} = -\frac{\Delta T}{\tau_D} + 2a \left(\frac{r_0}{R}\right)^2 \frac{\Delta \Theta}{\tau_S} \exp\left(-2\frac{t}{\tau_S}\right), \quad (24)$$

352 where the dimensionless constant

$$a = c_1 \frac{\eta_e}{\eta_S} \quad (25)$$

353 characterizes the proportion of heat effectively dissipated in the metal and τ_D
 354 the characteristic time of diffusion

$$\tau_D = \frac{c_2 R_{Fe}^2}{3\kappa}, \quad (26)$$

355 where c_2 , measuring in terms of R_{Fe} the thickness of the thermal boundary
 356 layer around the metal, $\delta = c_2 R_{Fe}$, is a dimensionless number.

357 Eq.24 cannot be used predictively in a complex situation as it requires the
 358 knowledge of various parameters c_1 , c_2 and a . The dependences of these param-
 359 eters with more fundamental quantities (mostly with the temperature depen-
 360 dence of the viscosity) have to be determined empirically. We will see however,
 361 that for a given choice of the rheology, Eq.24 captures the evolution of the
 362 metallic diapir temperature as a function of time and the dependence of this
 363 temperature with the diapir size. For example, Eq.24 suggests that the diffusion
 364 term decreases with R_{Fe} (as R_{Fe}^{-2} if one considers c_2 as a constant) while the
 365 dissipation term increases with R_{Fe}^2 . We can also use Eq.24 qualitatively by

366 assuming $a \sim c_1 \sim 4/15$ (using Stokes law) and $c_2 \sim 1$.

367 The expression Eq.24 shows that the temperature is not necessarily an in-
 368 creasing function of time. More precisely, according to Eq.24 the metal temper-
 369 ature increases just after the impact ($t \sim 0$), if

$$-\frac{\Delta T_0}{\tau_D} + 2a \left(\frac{r_0}{R}\right)^2 \frac{\Delta \Theta}{\tau_S} > 0 \quad (27)$$

370 Using the expressions for the temperature increase upon impact ΔT_0 (see Eq.1),
 371 the maximum temperature increase during segregation $\Delta \Theta$ (see Eq.21) and for
 372 the two time constant τ_S and τ_D (see Eq.13 and Eq.26), this condition implies
 373 that dissipative heating overcomes the conductive diffusion when

$$R_{Fe} > R_{Fe,min} \quad (28)$$

374 where $R_{Fe,min}$ involves the properties of the planet, but not its radius since
 375 ΔT_0 is proportional to R^2 :

$$R_{Fe,min}^4 = \frac{9}{8\pi} \left(\frac{r_0}{R}\right)^2 \frac{1}{c_1 c_2 a} \frac{\Delta T_0}{\Delta \Theta} \frac{\eta_S \kappa}{G \rho_0 (1 - f_0) \Delta \rho_0}. \quad (29)$$

376 According to the set of parameters shown in Table 1, $R_{Fe,min} \sim 45$ km
 377 (using $c_1 \sim a \sim 4/15$, $r_0 \sim R$ and $c_2 \sim 1$ but using values fitted from experi-
 378 ments does not change this radius very much for the moderate level of viscosity
 379 variations used in our simulations hereafter). Such a diapir corresponds to an
 380 impactor of radius $R_{imp} \sim 60$ km ($R_{imp} = R_{ic}/3^{1/3} = R_{Fe}/(3f_0)^{1/3}$). There-
 381 fore, only impactors larger than $R_{imp} = 60$ km generate metallic diapirs that
 382 heat up during sinking, although their initial temperature set by the impact is
 383 not dependent on the size of the impactor.

384 Integration of Eq.24 leads to:

$$\Delta T = \Delta T_0 \exp\left(-\frac{t}{\tau_D}\right) + a \left(\frac{r_0}{R}\right)^2 \Delta \Theta \frac{2\tau_D}{2\tau_D - \tau_S} \left(\exp\left(-\frac{t}{\tau_D}\right) - \exp\left(-2\frac{t}{\tau_S}\right) \right). \quad (30)$$

385 The initial temperature anomaly ΔT_0 decreases exponentially with time while
 386 the interplay between diffusion and dissipation controls the general temperature
 387 evolution. For the diapir to heat up, the heating time $\tau_S/2$ must be shorter
 388 than the diffusive time τ_D . Typically $r_0 \sim R$ and in the regime where the diapir
 389 heats up, the dissipation occurs before the diffusion, $\tau_S/2 \ll t \ll \tau_D$; the
 390 temperature rapidly increases to $\Delta T = \Delta T_0 + a (r_0/R)^2 \Delta \Theta$, and the physical
 391 interpretation of a is therefore the percentage of heat dissipated inside the metal.
 392 According to Eq.25, a should be lower than the coefficient c_1 of the Rybczinski-
 393 Hadamard velocity as the effective viscosity of the hot diapir η_e is likely lower
 394 than the average viscosity η_S . For a numerical application we take however
 395 $a \sim c_1 = 4/15 \sim 0.27$ as obtained for the isoviscous Rybczinski-Hadamard
 396 velocity. As $\Delta \Theta$ and ΔT_0 are simultaneously proportional to R^2 , the maximum
 397 temperature of the diapir is at most $\Delta T = 4.2 \Delta T_0$ and is independent of the
 398 planet size.

399 Dissipation decreases as $\exp(-2t/\tau_s) = (r/r_0)^2$ according to Eq.12. Hence,
 400 the dissipation term in Eq.24 decreases with depth. When a diapir heats up, its
 401 temperature increases therefore to the maximum ΔT_{max} reached at the radius
 402 r that satisfies $d\Delta T/dt = 0$ or

$$0 = -\frac{\Delta T_{max}}{\tau_D} + 2a \frac{\Delta \Theta}{\tau_S} \left(\frac{r}{R}\right)^2, \quad (31)$$

403 which implies

$$\left(\frac{r}{r_0}\right)^2 = \frac{\Delta T_{max}}{\Delta T_0} \left(\frac{R_{Fe,min}}{R_{Fe}}\right)^4. \quad (32)$$

404 The factor $\Delta T_{max}/\Delta T_0$ varies between 1 (no heating) and 4.2 (maximum esti-

405 mated temperature). As an example, an impactor of radius 120 km, generates
406 a metallic diapir of 96 km (two times $R_{Fe,min}$) that heats up until it reaches
407 half the radius of the impacted planet. The expression Eq.32 is only valid when
408 $R_{Fe} > R_{Fe,min}$, otherwise the diapir temperature simply decreases.

409 5. Numerical simulations

410 We compare the predictions of the analytical model to spherical axisymmet-
411 ric calculations of a sinking metallic drop, especially to extract the diffusive and
412 sinking times τ_D and τ_S and the fraction of heat trapped in the metallic phase
413 (e.g., the constants c_1 , c_2 and a , that we expect to be close to $4/15$, 1 and $4/15$).
414 We then compare these results to more complex numerical experiments where
415 a compositional anomaly is generated in the isobaric core after a large impact.
416 The effect of variable viscosity is also studied in these models.

417 5.1. Numerical models of sinking metallic drops

418 5.1.1. Sinking velocity

419 We solve numerically a set of problems in which we introduce metallic spheres
420 ($f_0 = 1$) of different sizes, tangent to the surface, in undifferentiated planets
421 ($f_0 = 0.17$) of various radii. From this set of experiments, we compare the
422 temporal evolution of the sphere position to what is predicted by Eq.12. The
423 calculations presented here are isoviscous for simplicity but variable viscosity
424 will be introduced in more complex cases. Fig.2 shows that the values of τ_S
425 obtained by fitting the center of the diapir position to an exponential in the
426 numerical models, vary as $1/R_{Fe}^2$ as expected from the analytical model, with
427 $c_1 = 0.187$ (almost 70% of the Hadamard-Rybczynski velocity for a homogenous
428 viscosity $4/15=0.27$). For large sphere radii, boundary effects are stronger and
429 the sinking times are slightly larger.

430 *5.1.2. Temperature evolution*

431 Large sinking diapirs heat up before cooling down by diffusion when the
432 velocity of the metal decreases sufficiently towards the center. Our theoretical
433 predictions given by Eq.30 are in good agreement with the computed evolutions
434 with the value c_1 obtained previously. Fig.3 shows the consistency between
435 the numerical results and the theory when the parameters c_2 and a are fitted
436 ($c_2 = 0.72$, $a = 0.2$ which is reasonably close to $c_1 = 0.187$). The value of a ,
437 indicates that 20% of the released heat is trapped in the metal. The maximum
438 temperature value, $2.2 \Delta T_0$, is in rough agreement with the estimate $\Delta T =$
439 $\Delta T_0 + a (r_0/R)^2 \Delta \Theta = 2.88 \Delta T_0$. This value is obtained for sufficiently large
440 impactors (> 200 km) since smaller ones can cool off very early upon sinking as
441 seen from Eq.32.

442 We monitor the temperature evolution for various diapir radii. Fitting the
443 temperature evolution with Eq.30 leads to values of τ_D and a for each diapir
444 radius. The corresponding characteristic diffusive times are plotted in Fig.4.
445 These times are consistent with analytical predictions from Eq.26 and increase
446 with the square of the diapir size. For all the experiments, the fraction of heat
447 a trapped in the metal is therefore reasonably constant ($\sim 22 \pm 5\%$) and close
448 to c_1 .

449 To verify condition Eq.32 that predicts the radius for which dissipation over-
450 comes diffusion, we computed the rate of heating or cooling of metallic spheres
451 as a function of their radius and depths. Various planetary radii have been used
452 and, as predicted, the heating always occur in the external part of the planet
453 (filled symbols). Near the center of the impacted planet, when the gravity de-
454 creases, diffusion dominates (open symbols) and the temperature of the sinking
455 metallic phase decreases. As shown in Fig.5, the transition between heating and
456 cooling occurs consistently within the shaded area predicted by the analytical

457 expressions Eq.32. For small diapirs ($R_{Fe} \leq 45$ km), diffusion dominates and
458 prevents heating. Large diapirs reach their maximum temperature and start
459 cooling near the high temperature estimate of the analytical model.

460 5.2. Application to global evolution after an impact

461 The thermo-chemical initial conditions after an impact differ from a simple
462 hot metallic sphere sinking within an undifferentiated material. Indeed, the
463 denser metallic pond collected at the bottom of the isobaric core is not spher-
464 ical and above it, a volume of light silicates rises and spreads underneath the
465 surface until it covers the entire surface of the planet. These deviations from
466 our analytical model potentially modify the results obtained from the sinking
467 metallic drop model. Here we show numerical simulations of segregation after
468 an impact and compare them to the analytical model previously developed.

469 Fig.6 depicts the thermal and compositional evolution after an impact of
470 a large impactor ($R = 4000$ km, $R_{imp} = 600$ km and $R_{Fe} = 480$ km). The
471 four rows correspond to real time snapshots at 0, 1.4, 3.8 and 546 Myrs. The
472 temperature field is depicted in the left column, and the composition in the right
473 column (undifferentiated material in light blue, metal in red, silicates in green).
474 The metallic pond sinks towards the center of the planet while heating. This
475 heating is in agreement with our previous findings that dissipation is larger than
476 diffusion for large impacts. However, the metal develops a tail through sinking
477 and is significantly deformed. In the meantime, the light silicates rise upward
478 and heat up as well, while stretching laterally to cover the whole surface of the
479 planet. Of course, the diffusion of heat out of the silicate layer near the surface,
480 is much faster than that out of the deep protocore and this shallow hot silicate
481 layer cools rapidly. On a much longer time scale (assuming unrealistically that
482 no other impact occurs, hot thermal plumes should start from the proto core-
483 mantle boundary and deliver the protocore heat to the surface (Behoukova and

484 Choblet, 2009).

485 Fig.7 illustrates the evolution of the conversion from potential to thermal
486 energy with time. During the thermo-chemical reequilibration, the potential
487 energy (thick line) decreases as the metal approaches the center and as the
488 silicates spread beneath the surface. Viscous heating induces an increase of
489 thermal energy (grey line). Once the metal has reached the center of the im-
490 pacted protoplanet, the thermal energy can only decrease. During this whole
491 process, heat is slowly removed by diffusion through the surface of the planet
492 and the cumulative heat flux (dotted line) balances the total energy budget.
493 This global balance (sum of potential energy, thermal energy and cumulative
494 heat flux (see Eq.14)) is closely satisfied which illustrates the good accuracy of
495 the numerical code.

496 We now introduce a temperature-dependence of the viscosity in the calcu-
497 lations. Experimental results suggest that the viscosity contrast between melt
498 iron and solid silicates can reach 20 orders of magnitude (Vocadlo et al., 2000).
499 Such a viscosity contrast is difficult to handle numerically and we use much
500 smaller values.

501 In our models, the viscosity varies as $\eta = \eta_0 \lambda^T$ and as the temperature of
502 metal may increase while sinking by a factor up to 2, it implies maximum viscos-
503 ity contrasts up to $1/\lambda^2$ orders of magnitude between cold and hot materials.
504 Using a composition dependent viscosity would have been more realistic but
505 viscous fronts are too difficult to handle numerically. We compare the thermo-
506 chemical states at the same time, $t = 3.2$ Myr for different viscosity factors in
507 Figure 8. We use $\lambda = 0.25$ (Figure 8 second row), $\lambda = 0.1$ (Figure 8 third row)
508 and $\lambda = 2.5 \times 10^{-2}$ (Figure 8 bottom row), the top row being the reference
509 isoviscous case.

510 Increasing the temperature-dependence of the viscosity softens the surround-

511 ing material around the metallic drop and the metallic diapir, at a given time,
 512 is closer to the center when its viscosity is decreased, as shown in Fig.8. How-
 513 ever, this effect remains small. Because the metallic pond becomes less viscous,
 514 its shape becomes more spherical and the tail developed in isoviscous exper-
 515 iments becomes thinner. Increasing the sinking velocity increases the rate of
 516 shear heating but not the total release of thermal energy which is only related
 517 to the change in gravitational energy. Lowering the viscosity in the surrounding
 518 material and within the metallic pond has also the effect of diminishing η_e . The
 519 dissipation is therefore increased in the undifferentiated material and decreased
 520 in the hot and less viscous metallic diapir. This effect combined with the faster
 521 spreading of the hot silicate that removes the heat more rapidly lead to lower
 522 maximum temperatures (see Fig.8).

523 We monitor the position of the inertia center of the metallic diapir as a
 524 function of time and compute the sinking times τ_S (see Figure 9). The position
 525 of the diapir obeys reasonably to the exponential law predicted by Eq.12. In the
 526 isoviscous case, the observed normalized time is $\tau_S = 563$ which is twice longer
 527 than what is predicted by Eq.13. This is due to the fact that the initial diapir
 528 shape is not spherical and to the presence of the rising volume of silicates. When
 529 the viscosity decreases with temperature the sinking is faster, $\tau_S = 249, 170$ and
 530 114 , for $\lambda = 0.25, 0.1$ and 2.5×10^{-2} (see Fig.9 and Tab.2). This is due to two
 531 effects: the reduction of viscosity inside the metal (the Rybczinski-Hadamard
 532 formula predicts an increase of the velocity factor c_1 from 0.27 to 0.33 when
 533 the interior viscosity of the diapir decreases) and the decrease of viscosity of the
 534 heated surrounding material.

535 In the experiments depicted in Fig.6 and Fig.8, the metal temperature in-
 536 creases and reaches a value close to twice the initial temperature of the isobaric
 537 core (Fig.10). However, heating within the metal is less pronounced with vari-

538 able viscosity and decreases with the viscosity contrast. Fitting the computed
539 temperature evolutions in the metallic diapirs with our theoretical model gives
540 values of c_2 in the isoviscous case and the variable viscosity cases (see Tab.2
541 and Fig.10). The thickness of the thermal boundary measured by c_2 decreases
542 with the sinking velocity (the Peclet number). The values of c_2 and of τ_D are
543 therefore related to $Pe^{-n} \propto \tau_S^n$ with an exponent $\sim 1/3$ in the range of values,
544 $n = 1/2 - 1/3$ predicted in Ribe (2007).

545 When the temperature dependence of the viscosity increases, the proportion
546 of energy heating the metal diapir, a , decreases (see Tab.2). As a consequence,
547 the heat release of the gravitational energy becomes increasingly efficient in the
548 surrounding undifferentiated material. This suggests that a diapir of very small
549 viscosity does not heat much during its motion while most of the release of
550 gravitational energy occurs in the undifferentiated materials. A low viscosity
551 diapir keeps basically its initial temperature because its characteristic diffusive
552 time is larger than its sinking time and also because of the buffering effect of
553 the temperature dependent viscosity (i.e., a too large cooling would increase the
554 viscosity and would bring back the dissipation within the diapir itself).

555 6. Discussion and conclusion

556 Core formation events induced by meteoritical impacts play a major role in
557 determining the early thermo-chemical state of growing planets. Large mete-
558 oritical impacts can trigger a local differentiation between metal and silicates
559 in a spherical zone above the surface called the isobaric core. The segregation
560 of dense and light phases through the undifferentiated material of the impacted
561 protoplanet induces a large viscous heating.

562 We followed the dynamics of the metal phase after a large impact with nu-
563 merical experiments in axisymmetrical spherical geometry. The sinking velocity

564 of the metal phase is Stokes-like and is function of the viscosity contrast be-
565 tween the metal phase and the undifferentiated crossed media. The velocity
566 increases when viscous heating decreases the viscosity of the surrounding ma-
567 terial. A stress dependent viscosity (not considered here) would also increase
568 this velocity (Samuel and Tackley, 2008). The sinking process in a planet with
569 a cold interior compared to its surface would eventually imply higher viscosity
570 contrasts between the metal and the surrounding material and would lead to
571 longer sinking times.

572 The gravitational energy release during the segregation is converted into vis-
573 cous heating in the metal and in the silicates. Our results show that a net viscous
574 heating of the metallic phase only occurs for large metallic diapirs ($R_{Fe} > 45$
575 km). This metallic volume at the bottom of the isobaric core would be produced
576 by an impactor of order $R_{imp} > 60$ km. This result underlines the importance
577 of accretion conditions on the inner thermal state of planetary bodies. Small
578 metallic diapirs cool while sinking and may ultimately bring the metal in a solid
579 state to the core of the impacted planet.

580 The heat repartition between the metal phase, the silicates and the undif-
581 ferentiated material is not only a function of the size of the metallic diapir
582 but also of the rheology of the various phases. For low viscosity of the metal
583 and of the sheared zone around the metallic diapir, the metal phase is weakly
584 heated. Hence, gravitational energy release will mainly lead to the heating of
585 the surrounding undifferentiated material and ultimately to its differentiation.

586 The viscosity variations that we explore in our simulations are of order
587 $\lambda^{\Delta T_{max}}$ which in the most extreme cases reach about four orders of magni-
588 tude over very short distances. This is certainly modest relative to the viscosity
589 contrasts of 20 orders of magnitude that exists between liquid metal and solid
590 silicates (Vocadlo et al., 2000). Viscosity contrasts based on composition rather

591 than temperature would be more realistic but would have occurred on even
592 shorter distances (the computation grid itself) that could not be resolved with
593 classical numerical methods. Our model is therefore an end-member of possible
594 models on heating modes during core formation. However the description of the
595 physics of the processes would still be valid for larger viscosity contrasts.

596 As soon as a growing planet reaches a few 1000 km in radius R , the heat-
597 ing by impacts becomes significant (the temperature increase varies as R^2 and
598 reaches 400 K for $R = 3000$ km, (Monteux et al., 2007)). This temperature
599 increase superimposed on the fossil temperature T_0 from short half-life radionu-
600 cleides (^{26}Al and ^{60}Fe) and previous impacts can lead to a temperature larger
601 than the melting temperature of the metallic phase. Our analytical models con-
602 firmed by numerical experiments show that the metallic drop reaches the planet
603 center in a time depending on the size of the metallic drop and the background
604 viscosity of the planet but not of its radius (see Eq.13). Even in the case where
605 the impacted planet is relatively cold and with a high viscosity of 10^{22} Pa s, this
606 time is smaller than a few million years for an impactor of 300 km. The sinking
607 timescales obtained in our models are comparable to those obtained with an
608 Arrhenius rheology (Ziethe and Spohn, 2007) and within the timeframe required
609 for an early core formation (< 60 My). The temperature increase in the undif-
610 ferentiated material localized along the sinking path of the metallic diapir could
611 provide a preferential low viscosity channel for the following differentiation events.

612 Proposing predictive models for the thermal consequences of differentiation
613 after an impact is fundamental in order to understand the thermal state of the
614 interior of growing planets. As shown in Ricard et al. (2009), core formation
615 of terrestrial protoplanets could be the consequence of a runaway segregation
616 induced by a large enough impact on undifferentiated material. These results
617 also underline the importance of accretionary conditions (size and temporal

618 repartition of impacts) on the thermal energy repartition and, hence, on the
619 magnetic history of growing planets (Elkins-Tanton et al., 2005).

620 **Acknowledgements**

621 The authors thank H. Samuel and M. Jellinek for helpfull discussions. The
622 authors also thank and H. Schmeling, T. Spohn and anonymous reviewers for
623 constructive comments. This project was funded by the A.N.R. ETHER.

624 **References**

625 Agee, C. B., 1997. Melting temperatures of the Allende meteorite: implications
626 for a Hadean magma ocean. *Phys. Earth Planet. Int.* 100, 41–47.

627 Behoukova, M., Choblet, G., 2009. Onset of convection in a basally heated
628 spherical shell, application to planets. *Earth Planet. Sci. Lett.*, submitted.

629 Christensen, U. R., Yuen, D. A., 1985. Layered convection induced by phase
630 transitions. *J. Geophys. Res.* 90, 10291–10300.

631 Croft, S. K., 1982. A first-order estimate of shock heating and vaporization
632 in oceanic impacts. Vol. 190. *Geological Implications of Impacts of Large
633 Asteroids and Comets on Earth*, edited by T.L. Silver and P.H. Schultz, Spec.
634 Pap. Geol. Soc. Am.

635 Davies, G. F., 1982. Ultimate strength of solids and formation of planetary
636 cores. *Geophys. Res. Lett.* 9, 1267–1270.

637 Douglas, J., 1955. On the numerical integration of $\frac{\partial^2 u}{\partial x^2} + \frac{\partial^2 u}{\partial y^2} = \frac{\partial u}{\partial t}$ by implicit
638 methods. *J. Soc. Ind. Appl. Math.* 3, 42–65.

639 Elkins-Tanton, L. T., Zaranek, S. E., Parmentier, E. M., Hess, P. C., 2005. Early
640 magnetic field and magmatic activity on Mars from magma ocean cumulate
641 overturn. *Earth Planet. Sci. Lett.* 236, 1–12.

642 Fei, Y., Bertka, C. M., Finger, L. W., 1997. High-Pressure Iron-Sulfur Com-
643 pound, Fe₃S₂, and Melting Relations in the FeFeS System. *Science* 275, 1621–
644 1623.

645 Flasar, F. M., Birch, F., 1973. Energetics of core formation: A correction. *J.*
646 *Geophys. Res.* 78, 6101–6103.

647 Gerya, T. V., Yuen, D. A., 2007. Robust characteristics method for modelling
648 multiphase visco-elastic thermo-mechanical problems. *Phys. Earth Planet.*
649 *Int.* 163, 83–105.

650 Ghosh, A., McSween, H. Y., 1998. A Thermal Model for the Differentiation of
651 Asteroid 4 Vesta, Based on Radiogenic Heating. *Icarus* 134, 187–206.

652 Golabek, G. J., Schmeling, H., Tackley, P. J., 2008. Earth’s core formation
653 aided by flow channelling instabilities induced by iron diapirs. *Earth Planet.*
654 *Sci. Lett.* 271, 24–33.

655 Hadamard, J., 1911. Mouvement permanent lent d’une sphère liquide et
656 visqueuse dans un liquide visqueux. *C. R. Acad. Sci.* 152, 1735–1738.

657 Hewitt, J. M., McKenzie, D. P., Weiss, N. O., 1975. Dissipative heating in
658 convective flows. *Journal of Fluid Mechanics* 68, 721–738.

659 Höink, T., Schmalzl, J., Hansen, U., 2005. Formation of compositional structures
660 by sedimentation in vigorous convection. *Phys. Earth Planet. Int.* 153, 11–20.

661 Honda, R., Mizutani, H., Yamamoto, T., 1993. Numerical simulation of Earth’s
662 core formation. *J. Geophys. Res.* 98, 2075–2090.

663 Kleine, T., Münker, C., Mezger, K., Palme, H., 2002. Rapid accretion and early
664 core formation on asteroids and the terrestrial planets from Hf-W chronome-
665 try. *Nature* 418, 952–955.

- 666 Laney, C. B., 1998. Computational gasdynamics. Cambridge University Press,
667 Cambridge.
- 668 Monteux, J., 2009. Modélisation numérique de la formation du noyau ter-
669 restre : contribution des impacts météoritiques. Ph.D. thesis, Université
670 Claude Bernard Lyon 1.
- 671 Monteux, J., Coltice, N., Dubuffet, F., Ricard, Y., 2007. Thermo-mechanical
672 adjustment after impacts during planetary growth. *Geophys. Res. Lett.* 34,
673 24201–24205.
- 674 O’Keefe, J. D., Ahrens, T. J., 1977. Impact-induced energy partitioning, melt-
675 ing, and vaporization on terrestrial planets. In: Merrill, R. B. (Ed.), *Lun.*
676 *Planet. Sci. Conf.* Vol. 8. pp. 3357–3374.
- 677 Peaceman, D. W., Rachford, H. H., 1955. The numerical solution of parabolic
678 and elliptic differential equations. *J. Soc. Ind. Appl. Math.* 3, 28–41.
- 679 Pierazzo, E., Vickery, A. M., Melosh, H. J., 1997. A Reevaluation of Impact
680 Melt Production. *Icarus* 127, 408–423.
- 681 Ratcliff, J. T., Tackley, P. J., Schubert, G., Zebib, A., 1997. Transitions in
682 thermal convection with strongly variable viscosity. *Phys. Earth Planet. Int.*
683 102, 201–212.
- 684 Ribe, N. M., 2007. Analytical Methods in Mantle Dynamics, *Treatise of Geo-*
685 *physics.* Vol. 7. Schubert, G. editor in Chief, Elsevier.
- 686 Ricard, Y., 2007. Physics of Mantle Convection, *Treatise of Geophysics.* Vol. 7.
687 Schubert, G. editor in Chief, Elsevier.
- 688 Ricard, Y., Sramek, O., Dubuffet, F., 2009. A multi-phase model of runaway
689 core-mantle segregation in planetary embryos. *Earth Planet. Sci. Lett.*, in
690 press.

691 Roe, P. L., 1986. Characteristic-based schemes for the Euler equations. Annual
692 Review of Fluid Mechanics 18, 337–365.

693 Rybczynski, W., 1911. über die fortschreitende bewegung einer flüssigen kugel
694 in einen medium. Bull. Acad. Sci. Cracovie 1, 40–46.

695 Samuel, H., Tackley, P. J., 2008. Dynamics of core formation and equilibration
696 by negative diapirism. *Geochem. Geophys. Geosyst.* 9, 6011–6026.

697 Schubert, G., Turcotte, D. L., Olson, P., Sep. 2001. Mantle convection in the
698 Earth and planets. Cambridge University Press.

699 Senshu, H., Kuramoto, K., Matsui, T., 2002. Thermal evolution of a growing
700 Mars. *J. Geophys. Res.* 107, 1–13.

701 Shannon, M. C., Agee, C. B., 1996. High pressure constraints on percolative
702 core formation. *Geophys. Res. Lett.* 23, 2717–2720.

703 Sramek, O., 2007. Modèle d’écoulement biphasé en sciences de la terre: fu-
704 sion partielle, compaction et différenciation,. Ph.D. thesis, Ecole Normale
705 Supérieure de Lyon.

706 Stevenson, D. J., 1989. Formation and early evolution of the Earth. in *Mantle*
707 *convection and plate tectonics*, W.R. Peltier, ed.

708 Stevenson, D. J., 1990. Fluid dynamics of core formation. *Origin of the Earth*
709 edited by H. E. Newsom and J. H. Jones, eds., Oxford Univ., New York.

710 Tonks, W. B., Melosh, H. J., 1992. Core formation by giant impacts. *Icarus* 100,
711 326–346.

712 Touboul, M., Kleine, T., Bourdon, B., Palme, H., Wieler, R., 2007. Late forma-
713 tion and prolonged differentiation of the Moon inferred from W isotopes in
714 lunar metals. *Nature* 450, 1206–1209.

- 715 Vocadlo, L., Alfè, D., Price, G. D., Gillan, M. J., 2000. First principles calcula-
716 tions on the diffusivity and viscosity of liquid Fe-S at experimentally accessible
717 conditions. *Phys. Earth Planet. Int.* 120, 145–152.
- 718 Von Bargen, N., Waff, H. S., 1986. Permeabilities, interfacial areas and cur-
719 vatures of partially molten systems: Results of numerical computations of
720 equilibrium microstructures. *J. Geophys. Res.* 91, 9261–9276.
- 721 Yin, Q., Jacobsen, S. B., Yamashita, K., Blichert-Toft, J., Télouk, P., Al-
722 barède, F., 2002. A short timescale for terrestrial planet formation from Hf-W
723 chronometry of meteorites. *Nature* 418, 949–952.
- 724 Yoshino, T., Walter, M. J., Katsura, T., 2003. Core formation in planetesimals
725 triggered by permeable flow. *Nature* 422, 154–157.
- 726 Ziethe, R., Spohn, T., 2007. Two-dimensional Stokes flow around a heated cylin-
727 der: A possible application for diapirs in the mantle. *J. Geophys. Res.* 112,
728 1–13.

Table 1: Typical parameter values for numerical models

Planet radius	R	1000 - 4000 km
Impactor radius	R_{imp}	100 - 400 km
Silicate density	ρ_{Si}	3500 kg m ⁻³
Iron density	ρ_{Fe}	8000 kg m ⁻³
Density difference	$\Delta\rho_0 = \rho_{Fe} - \rho_{Si}$	4500 kg m ⁻³
Average density	$\frac{\rho_0}{2}$	4270 kg m ⁻³
Heat capacity	ρC_p	4×10^3 kJ K ⁻¹ m ⁻³
Heat diffusivity	κ	10 ⁻⁶ m ² s ⁻¹
Thermal conductivity	k	4 W m ⁻¹ K ⁻¹
Initial temperature	T_0	K
Metal content	f_0	0.17
Viscosity	η_0	10 ²² Pa s
Viscosity factor	λ	$2.5 \times 10^{-2} - 1$
Gravity	$g_0 = 4\pi G \rho_0 R/3$	m s ⁻²
Stokes velocity scale	$\Delta\rho_0 g_0 R^2 / \eta_0$	~100 m/yr
Time scale	$\eta_0 / \Delta\rho_0 g_0 R$	~20 kyr
Rayleigh number Ra_χ	$\frac{\rho C_p \Delta\rho_0 g_0 R^3}{\eta_0 k}$	~10 ⁸
Buoyancy B	$\Delta\rho_0 / \alpha \rho_0 \Delta T_0$	25-250
Dissipation number D_χ	$\Delta\rho_0 g_0 R / \rho C_p \Delta T_0$	36.6
Impact energy conversion coefficient	γ	0.3
Volume effectively heated by impact	$h(m)$	2.7
Stokes velocity coefficient	c_1	0.1-0.2
Heat diffusion coefficient	c_2	0.3-1.05

Table 2: Values obtained fitting numerical experiments with theoretical predictions (Eq.12 and Eq.30) for different values of λ (with $R = 2000$ km and $R_{imp} = 300$ km)

	$\lambda = 1$	$\lambda = 0.25$	$\lambda = 0.1$	$\lambda = 2.5 \times 10^{-2}$
τ_S	563	249	170	114
τ_D	20 054	16 520	13 316	8974
a	19%	14.7%	11%	7%

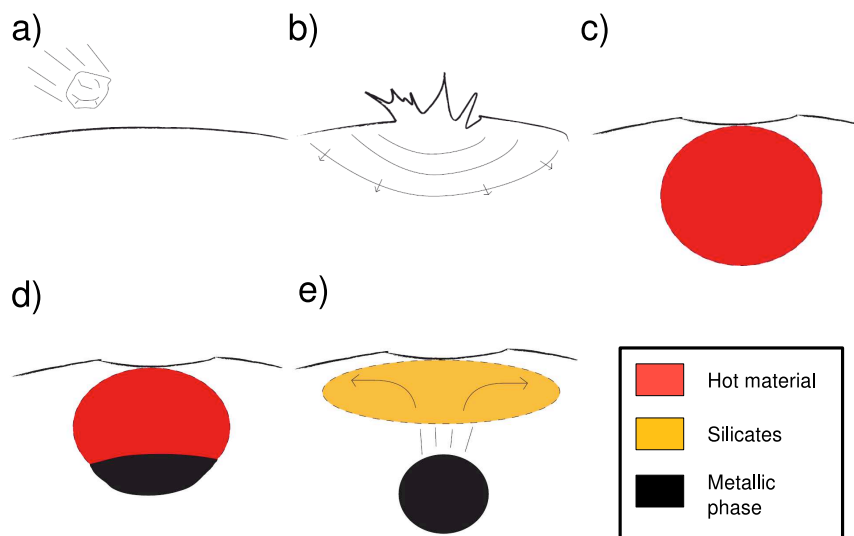


Figure 1: Schematic view of the chemical equilibration following a large impact on an undifferentiated protoplanet. In the isobaric core resulting from the dissipation of the shock wave (a,b), the temperature increase (c) melts the metal that segregates rapidly (d), then sinks toward the planetary embryo center by a diapiric instability (e).

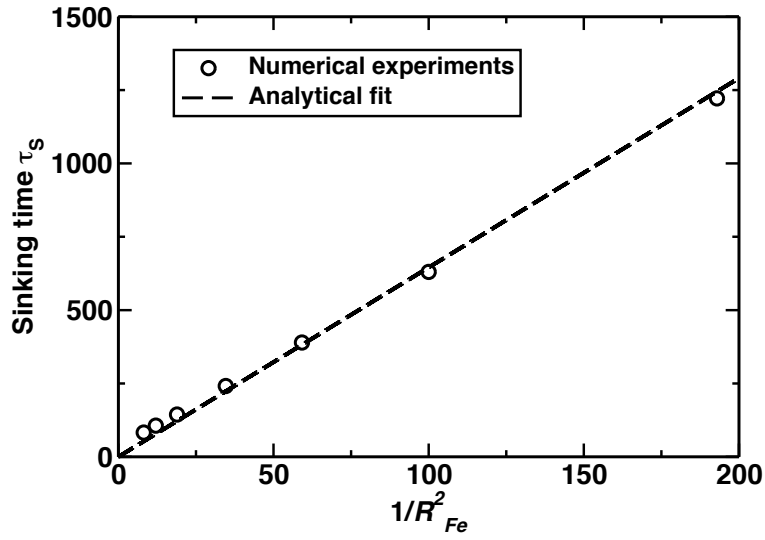


Figure 2: Characteristic sinking time τ_S as a function of $1/R_{Fe}^{*2}$, where R_{Fe}^* is the non-dimensionalized metallic sphere radius. Results from numerical experiments (with uniform viscosity $\eta_S = 10^{22}$ and $R = 1000$ km) are represented with black circles. Theoretical fit from Eq.13 is shown by the dashed line with $c_1 = 0.187$.

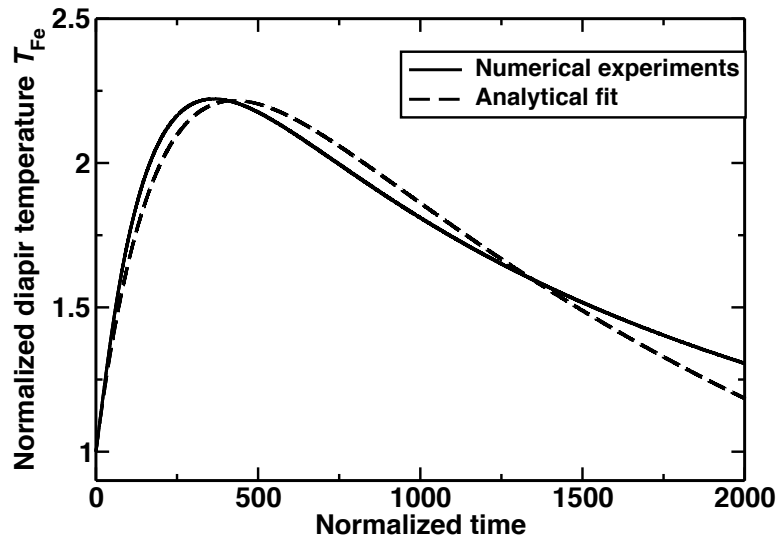


Figure 3: Temperature evolution (black line) of a metallic sphere ($R_{Fe} = 130$ km) falling in an undifferentiated planet with $R = 1000$ km. Theoretical evolution from Eq.30 is shown with a dashed line ($c_1 = 0.187$, $c_2 = 0.72$ and $a = 20\%$).

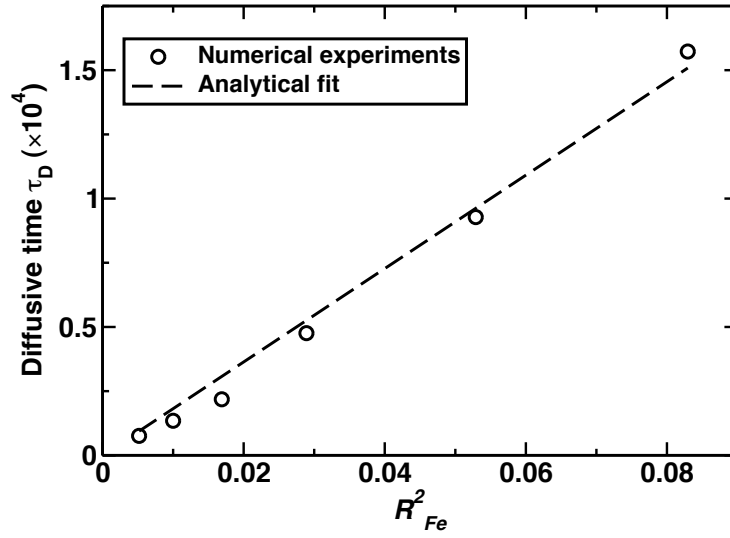


Figure 4: Non-dimensional characteristic time of diffusion τ_D as a function of the non-dimensionalized metallic sphere radius. Results from numerical experiments (with a uniform viscosity and $R = 1000$ km) are represented with black circles. Theoretical fit from Eq.26 is shown in dashed line with $c_2 = 1.01$.

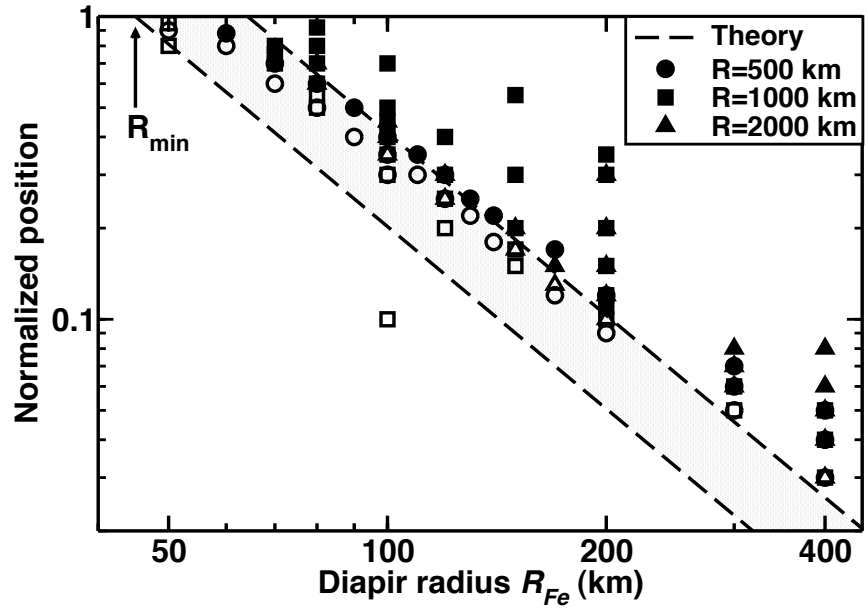


Figure 5: Thermal behaviour of a sinking metal sphere in an undifferentiated media as function of position and sphere radius. Each symbol represents the instantaneous thermal behaviour of an hot metallic sphere with radius R_{Fe} for a given initial position. Filled symbols represent numerical experiments with viscous heating and open symbols represent numerical experiments with only cooling. Different symbols characterize different planets radii. The analytical transition between heating and cooling is predicted within the shaded area and the borders of this area are defined with $\Delta T_{max}/\Delta T_0$ between 1 (no heating) and 4.2 (maximum heating)(see, Eq.32).

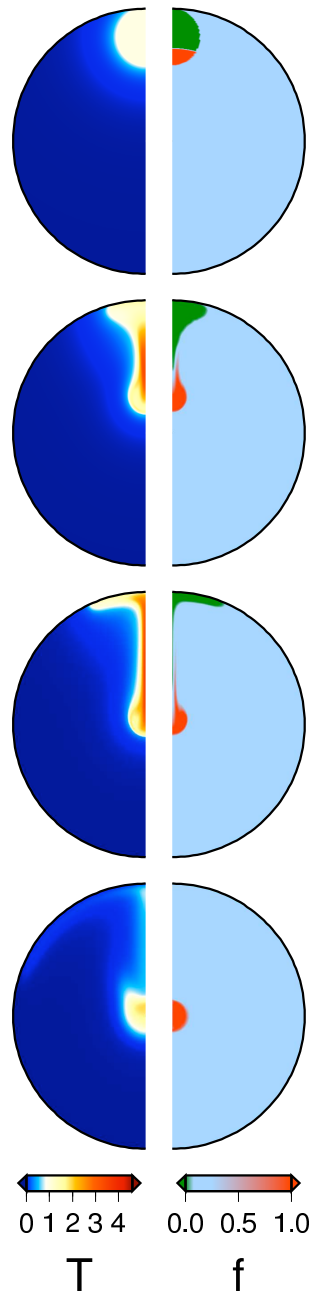


Figure 6: Non dimensional temperature (left) and composition (right) at times $t = 0$ (first line), $t = 1.4$ My (second line), $t = 3.8$ My (third line) and $t = 546$ My (fourth line) (computed for a uniform viscosity with $R = 4000$ km, $R_{imp} = 600$ km and 200×200 grid points)

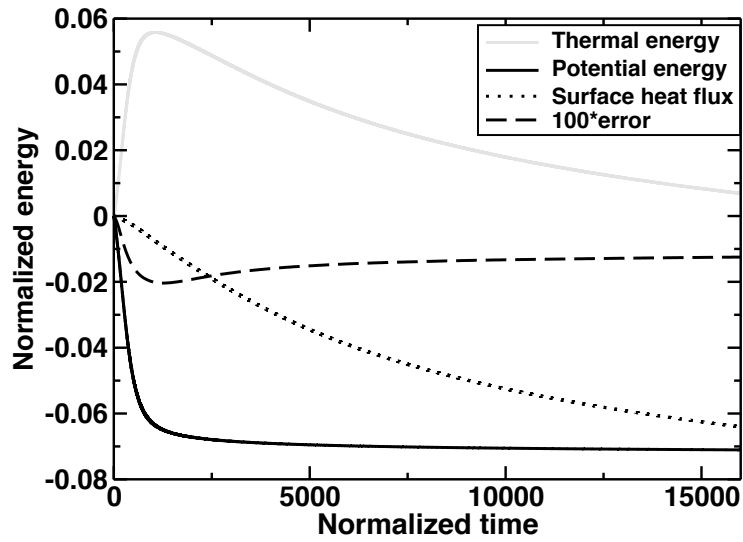


Figure 7: Non dimensionalized potential (solid black line) and thermal (solid grey line) energies and time integrated surface heat flow (dotted black line) as functions of time. The sum of these three quantities times 100 is shown in dashed black line. Its difference to zero is indicative of the accuracy of the energy conservation of the numerical code (for $R = 2000$ km, $R_{imp} = 300$ km and $R_{Fe} = 240$ km and uniform viscosity).

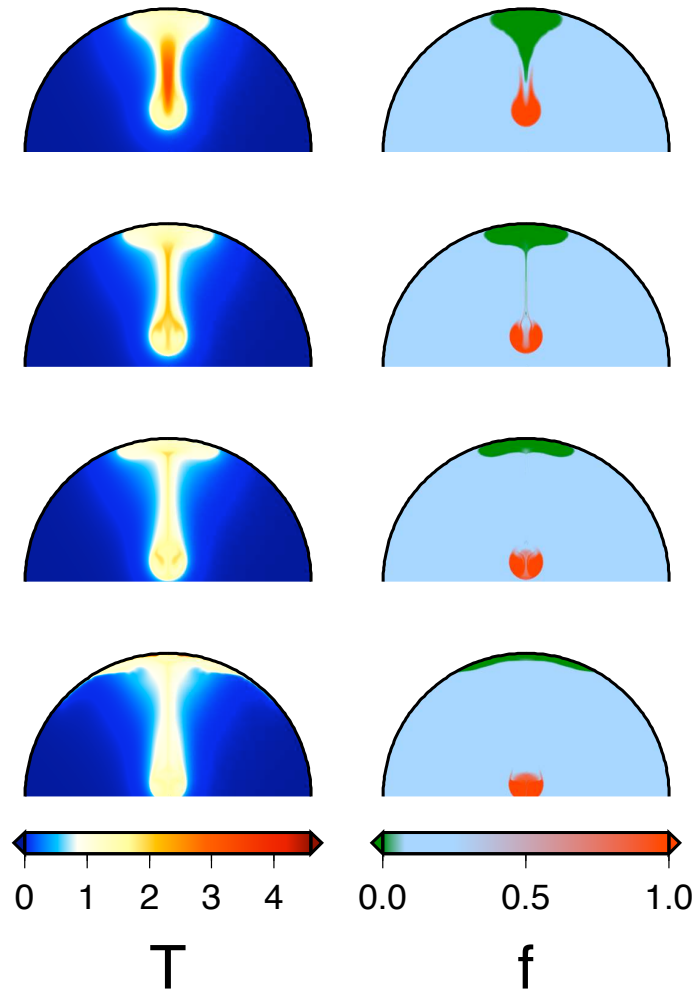


Figure 8: The four rows depict the temperature (left) and the composition (right) at $t = 3.2$ My (with $R = 2000$ km and $R_{imp} = 300$ km), for a uniform viscosity (top) and for variable viscosities (contrast of ~ 16 (second row), ~ 100 (third row) and ~ 1600 (bottom row)). As expected, the sinking velocity of the metallic diapir and the rising velocity of the silicates, both increase when their viscosity is decreased.

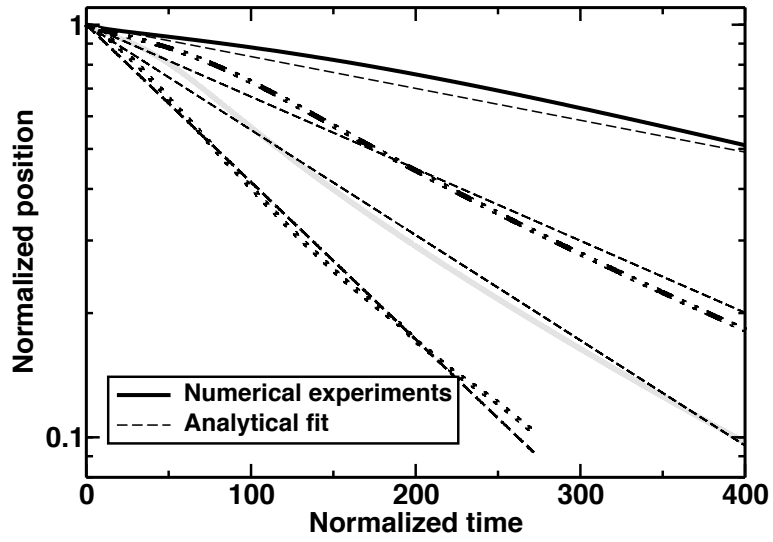


Figure 9: Position of the inertia center of the metal phase as a function of time for a uniform viscosity (black line) and for temperature-dependent viscosities with $\lambda = 0.25$ (dashed dotted line), $\lambda = 0.1$ (grey line) and $\lambda = 2.5 \times 10^{-2}$ (dotted line) ($R = 2000$ km and $R_{imp} = 300$ km). Thin dashed lines correspond to simple exponential fittings from which the sinking times are extracted (see Tab.2).

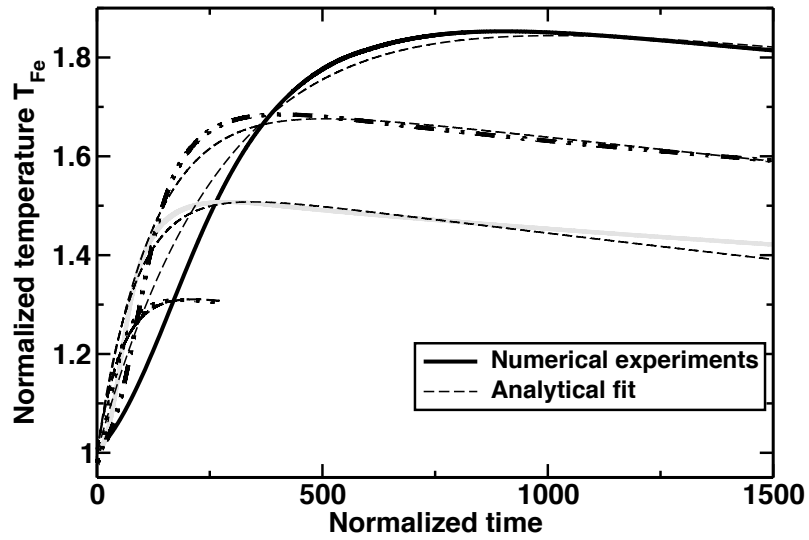


Figure 10: Temperature evolution of the metal phase as a function of time for a uniform viscosity (solid black line) and for temperature-dependent viscosities with $\lambda = 0.25$ (dashed dotted line), $\lambda = 0.1$ (grey line) and $\lambda = 2.5 \times 10^{-2}$ (dotted line) ($R = 2000$ km and $R_{imp} = 300$ km). Thin dashed lines correspond to theoretical results from Eq.30 from which the diffusive times and the proportion of energy heating the metal diapir are extracted (see Tab.2).